

Fractional vortices and Ising superconductivity in multiband superconductors

Haijiao Ji^{1,2} and Noah F. Q. Yuan^{1,2,*}

¹*Tsung-Dao Lee Institute, Shanghai Jiao Tong University, Shanghai 201210, China*

²*School of Physics and Astronomy, Shanghai Jiao Tong University, Shanghai 200240, China*

Inspired by the recent experiments in monolayer iron-based superconductors, we theoretically investigate properties of a two-dimensional multiband superconductor, focusing on two aspects. First, for vortex bound states, the spatial anisotropy and positions of electron density peaks are associated with interband couplings. Second, even with inversion symmetry, there allows a Ising-type spin-orbit coupling, leading to the enhanced in-plane upper critical field.

Introduction.— Recently, multiband superconductors with multi-component order parameters attract growing attention in the condensed matter community, with material candidates such as MgB₂ [1–5], NbSe₂ [6–10] and Ba_{1-x}K_xFe₂As₂ [11–16]. It has been proposed that multiband superconductors may lead to exotic forms of superconductivity such as topological superconductivity [17–19] and quantum vortices [20, 21], with several experimental progress reported [3, 4, 7, 9, 13, 22, 23].

In particular, the recent experimental observation of evidence on quantum vortices carrying fractional flux quantum (so-called *fractional vortices*) in iron-based superconductors by Y. Zheng, *et al.* [24] adds fuel to the study of multiband superconductivity.

Theoretically multiband superconductivity can be analyzed within the phenomenological Ginzburg-Landau framework [25–30], and self-consistent calculations based on microscopic band structures [31–35]. To understand the observations of fractional vortices and multiband superconductivity reported in Ref. [24], one first needs to analyze the microscopic band structure of iron-based superconductors.

It is generally recognized that the Fermi surfaces of iron-based superconductors mainly consist of *d*-orbital pockets of iron atoms, hybridized with orbitals from other atoms [36–43]. In particular for KFe₂As₂ in Ref. [24], one may focus on hole pockets from d_{xz} , d_{yz} and d_{xy} orbitals near Γ , M points [44–48], and the point group is D_{4h} .

In this work, we consider a two-dimensional (2D) superconductor model with d_{xz} , d_{yz} and d_{xy} -orbital hole bands under point group D_{4h} . First, we focus on the two-band model near Γ point formed by d_{xz} , d_{yz} -bands. After deriving the $k \cdot p$ model from symmetry analysis, we investigate the anisotropy of Fermi contours and vortex bound states. Then, we extend to the three-band model of d_{xz} , d_{yz} and d_{xy} bands, and discuss the corresponding modifications due to the additional d_{xy} -band. Finally, we self-consistently calculate the in-plane upper critical field of the multiband superconductor.

Two-band model.— At Γ point, d_{xz} , d_{yz} orbitals furnish the 2D irreducible representation E_g of point group D_{4h} . In particular, under in-plane fourfold rotation C_{4z} , we

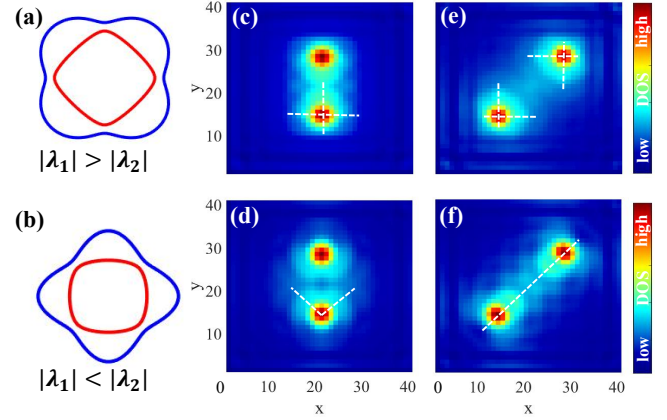


FIG. 1. (a, b) Fermi contours and (c-f) zero-energy density of states in two-band model Eq. (3). Dashed lines denote the directions with longer decay length. The two-band model Eq. (3) is employed with $\mu = -0.6$, $t = -1$, $\beta = 0$, $\Delta_1 = \Delta_2 = 0.1$. In (c,e), $\lambda_1 = 0.2$, $\lambda_2 = 0.1$ and in (d,f), $\lambda_1 = 0.1$, $\lambda_2 = 0.2$. Fractional vortices are described by Eq. (11) with $\xi = 1$.

find the eigenbasis of the orbital angular momentum L_z

$$d_{\pm} \equiv \frac{1}{\sqrt{2}}(d_{xz} \pm id_{yz}), \quad L_z = \pm 1. \quad (1)$$

On the spinful orbital basis $\{d_{+\uparrow}, d_{+\downarrow}, d_{-\uparrow}, d_{-\downarrow}\}$, the time-reversal symmetry \mathcal{T} , in-plane fourfold rotation symmetry C_{4z} , and vertical (horizontal) mirror symmetry M_y (M_z) are represented as ($J_z = \sigma_z + \frac{1}{2}s_z$)

$$\mathcal{T} = is_y\sigma_x K, \quad C_{4z} = i^J_z, \quad M_y = is_y\sigma_x, \quad M_z = is_z, \quad (2)$$

where \mathbf{s} are Pauli matrices in spin space, $\boldsymbol{\sigma}$ in orbital space, and K is the complex conjugation operator.

Since we have both orbital and spin degrees of freedom, we expect two types of couplings, namely the interband coupling (IBC) between different orbitals, and the spin-orbit coupling (SOC) between different spins.

By method of invariants, the normal Hamiltonian up to the quadratic order of electron momentum reads

$$H_0(\mathbf{k}) = \varepsilon + 2\lambda_1 k_x k_y \sigma_y + \lambda_2 (k_x^2 - k_y^2) \sigma_x + \beta s_z \sigma_z \quad (3)$$

where $\mathbf{k} = (k_x, k_y)$ is the electron momentum, ε is the kinetic term, λ_1, λ_2 are spin-independent IBC parameters,

and β is the Ising SOC. For hole bands we have

$$\varepsilon = -\mu - tk^2, \quad (4)$$

with chemical potential $\mu < 0$ and hopping term $t < 0$.

Under time-reversal symmetry, \mathbf{s}, σ_z are odd, while $\sigma_{x,y}$ are even. Under inversion, \mathbf{s}, σ are all even. As a result, both IBCs and Ising SOC are even in \mathbf{k} , unlike those \mathbf{k} -odd IBCs in Benervig-Hughes-Zhang (BHZ) model[49] and \mathbf{k} -odd Rashba SOC[50, 51].

Unlike the isotropic kinetic term ε and Ising SOC β , IBCs $\lambda_{1,2}$ serve as the source for anisotropy in our model. The normal Hamiltonian has the emergent symmetry

$$(k_x, k_y) \rightarrow \frac{1}{\sqrt{2}}(k_x + k_y, k_x - k_y), \quad \lambda_1 \leftrightarrow \lambda_2. \quad (5)$$

Namely, an in-plane improper rotation of angle $\pi/4$ is equivalent to the exchange of $\lambda_{1,2}$. When $|\lambda_1| = |\lambda_2|$, the model acquires an emergent full rotation symmetry.

The anisotropy of Fermi contours in the normal Hamiltonian depends on λ_1, λ_2 as shown in Fig. 1(a) and (b). When $|\lambda_1| > |\lambda_2|$, the outer pocket is “ \times ”-shape (d_{xy} -like) as in Fig. 1(a), and when $|\lambda_1| < |\lambda_2|$ it is “+”-shape ($d_{x^2-y^2}$ -like) as in Fig. 1(b). In fact, with $\lambda_{\pm}^2 \equiv \frac{1}{2}(\lambda_1^2 \pm \lambda_2^2)$, the bands of Eq. (3) read

$$E_{\pm}(\mathbf{k}) = \varepsilon \pm \sqrt{(\lambda_+^2 - \lambda_-^2 \cos 4\theta)k^4 + \beta^2}, \quad (6)$$

in the polar coordinate $\mathbf{k} = k(\cos \theta, \sin \theta)$.

In the next session, we discuss the anisotropy effects of IBCs $\lambda_{1,2}$ in superconductivity.

Superconductivity.— We now turn to the superconducting phase of our model, and discuss both uniform pairing and the non-uniform vortices.

When the pairing is uniform in real space, we can work in the momentum space, where the electron operator $d_{\sigma s}$ carries orbital $\sigma = \pm$, spin $s = \uparrow, \downarrow$ and momentum \mathbf{k} , while the hole operator $d_{\sigma s}^\dagger$ carries orbital $-\sigma$, spin $-s$ and momentum $-\mathbf{k}$. The Bogouliubov-de Gennes (BdG) Hamiltonian on the Nambu basis $\{d_{+\uparrow}, d_{-\uparrow}, d_{+\downarrow}, d_{-\downarrow}, d_{+\uparrow}^\dagger, d_{-\uparrow}^\dagger, d_{+\downarrow}^\dagger, d_{-\downarrow}^\dagger\}^T$ is

$$H_{\text{BdG}}(\mathbf{k}) = \begin{pmatrix} H_0(\mathbf{k}) & \Delta(\mathbf{k}) \\ \Delta^\dagger(\mathbf{k}) & -H_0^*(-\mathbf{k}) \end{pmatrix}. \quad (7)$$

The pairing matrix $\Delta(\mathbf{k})$ includes spin-singlet, spin-triplet, intraband and interband channels, and the particle-hole symmetry reads

$$\Delta(\mathbf{k}) = -\Delta^T(-\mathbf{k}). \quad (8)$$

In the following, we consider on-site pairings, which are described by an anti-symmetric pairing matrix

$$\Delta = \begin{pmatrix} 0 & \Delta_+ & \Delta_0 + \Delta_z & \Delta_1 \\ -\Delta_+ & 0 & \Delta_2 & \Delta_0 - \Delta_z \\ -\Delta_0 - \Delta_z & -\Delta_2 & 0 & \Delta_- \\ -\Delta_1 & -\Delta_0 + \Delta_z & -\Delta_- & 0 \end{pmatrix} \quad (9)$$

with six pairing order parameters $\Delta_{1,2}$, $\Delta_{0,z}$ and Δ_{\pm} , which furnish four irreducible representations of D_{4h}

$$\Delta_{1,2} \in A_{1g}, \quad \Delta_0 \in B_{1g}, \quad \Delta_z \in B_{2g}, \quad \{\Delta_+, \Delta_-\} \in E_g. \quad (10)$$

In phase B_{1g} or B_{2g} , there is only one order parameter and multiband superconductivity cannot be realized. In phase E_g , the two order parameters Δ_{\pm} are degenerate in the quadratic Ginzburg-Landau (GL) free energy, but have to fall into either chiral ($\Delta_+ \Delta_- = 0$) or nematic ($|\Delta_+| = |\Delta_-|$) phase when considering quartic GL terms.

We thus consider the trivial pairing phase A_{1g} , which is time-reversal-invariant and pairs up opposite-spin opposite-orbital states. It can be found that the BdG bands of Eq. (7) are topologically trivial, which is consistent with experimental observations in iron-based superconductors that edge states are absent [24].

We then move to the non-uniform pairings in the real space. Namely, $\Delta_{1,2}(\mathbf{r})$ can now depend on the spatial position \mathbf{r} . In particular we focus on fractional vortices. For simplicity, a fractional vortex for order parameter Δ_j to vanish at its core $\mathbf{r} = \mathbf{c}_j$ can be modeled by the ansatz

$$\Delta_j(\mathbf{r}) = \Delta_j e^{i\varphi} \tanh \frac{|\mathbf{r} - \mathbf{c}_j|}{\xi}, \quad (11)$$

where ξ is coherent length, φ is the polar angle of $\mathbf{r} - \mathbf{c}_j$, and Δ_j is the asymptotic pairing amplitude away from the core $|\mathbf{r} - \mathbf{c}_j| \rightarrow \infty$. The magnetic flux trapped in such a fractional vortex is a fraction of the flux quantum and hence the name [20–24].

With the above ansatz, one can calculate the bound states within fractional vortices, which can be represented by the zero-energy density of states as shown in Fig. 1(c-f). From the calculations, one can find that the vortex bound states (VBSs) are usually localized near the fractional vortex core with anisotropic decay length.

It is usually found that, the VBS decay length is longer along x and y axes when $|\lambda_1| > |\lambda_2|$ [Fig. 1(c) and (e)], along diagonal directions $|x| = |y|$ when $|\lambda_1| < |\lambda_2|$ [Fig. 1(d) and (f)]. We may understand these in terms of effective pairing potentials on the Fermi contours $E_{\pm} = 0$. It can be worked out that due to the d -wave-like IBCs $\lambda_{1,2}$, effective pairings on the Fermi contours are also d -wave-like with the form factor $-2i\lambda_1 k_x k_y + \lambda_2(k_x^2 - k_y^2)$. When $|\lambda_1| > |\lambda_2|$, the effective pairings are more like d_{xy} -wave with x and y axes as weaker pairing directions, and when $|\lambda_1| < |\lambda_2|$, the effective pairings are more like $d_{x^2-y^2}$ -wave with diagonal directions $|x| = |y|$ as weaker pairing directions. Along weaker pairing directions, VBSs will be less bounded and the decay length is longer.

The relation between anisotropy of Fermi contours and that of VBSs obtained in our ansatz-based calculations can also be found in self-consistent calculations [31].

Three-band model.— As mentioned previously, the additional d_{xy} -orbital hole band can hybridize with d_{\pm} -bands, and the two-band model Eq. (3) becomes a three-band model, which is a 6 by 6 matrix including spin.

At either Γ or M point, the point group is D_{4h} , and d_{xy} -orbital furnishes the 1D irreducible representation B_{2g} . In particular under C_{4z} its orbital angular momentum is $L_z = 2$, and under M_y it changes sign. Since inversion symmetry is preserved in D_{4h} , there is no SOC for the single-band d_{xy} -orbital. As a result, the dispersion of d_{xy} -band can be described by a scalar function $\varepsilon'(\mathbf{k})$, which is \mathbf{k} -even kinetic term.

Near M point, IBCs between d_{xy} -band and d_{\pm} -bands are negligible to the leading order, due to the large momentum/energy mismatch. We may treat d_{xy} -band as an additional band at M point, which is decoupled from d_{\pm} -bands and hence does not affect the previous results in this manuscript.

Near Γ point, due to time-reversal symmetry, the three-band Hamiltonian including SOC reads

$$H_0(\mathbf{k}) = \begin{pmatrix} h(\mathbf{k}) & 0 \\ 0 & h^*(-\mathbf{k}) \end{pmatrix}, \quad (12)$$

on the basis $\{d_{+\uparrow}, d_{-\uparrow}, d_{xy\uparrow}, d_{-\downarrow}, d_{+\downarrow}, d_{xy\downarrow}\}$ with

$$h = \begin{pmatrix} \varepsilon + \beta & \lambda & A_+ \\ \lambda^* & \varepsilon - \beta & A_- \\ A_+^* & A_-^* & \varepsilon' \end{pmatrix}. \quad (13)$$

To the leading order, we have $\varepsilon(\mathbf{k}) = -\mu - tk^2$, and $\lambda(\mathbf{k}) = -2i\lambda_1 k_x k_y + \lambda_2(k_x^2 - k_y^2)$ as in the two-band model Eq. (3). The IBCs between d_{\pm} -bands and d_{xy} -band are

$$A_{\pm}(\mathbf{k}) = a_{\pm}(k_x \pm ik_y), \quad a_{\pm} \in \mathbb{C}. \quad (14)$$

Under in-plane rotations, d_{\pm} -orbitals are fully isotropic, while d_{xy} -orbital is fourfold anisotropic. Thus, unlike fully isotropic $\varepsilon(\mathbf{k})$, we expect $\varepsilon'(\mathbf{k})$ is fourfold anisotropic

$$\varepsilon'(\mathbf{k}) = -\mu + M - t'k^2 - t''(k^4 + \eta k_x^2 k_y^2). \quad (15)$$

For comparison, the fourfold anisotropy of d_{\pm} -bands is due to the IBC $\lambda(\mathbf{k})$ within d_{\pm} -bands as shown in Eq. (6), and a two-band Hamiltonian Eq. (3) up to the quadratic terms in \mathbf{k} is sufficient to describe such anisotropy.

When μ is near the gap between ε and ε' , $|\mu| \sim |M|$, close to the Fermi energy, the significant bands are d_{xy} -band and one of d_{\pm} -bands, leading to the two-band BHZ model, as derived in monolayer $\text{FeTe}_{1-x}\text{Se}_x$ [19].

On the contrary, deep in the hole band, $|\mu| \gg |M|$, the three-band model Eq. (13) has to be employed. In this case, one may investigate the role of IBCs in the Fermi contour anisotropy. It can be found that, when $\lambda_1 + \lambda_2 = 0$ and $\eta = 0$, all three Fermi contours are circular and fully isotropic in the three-band model Eq. (13), which is a special case of the isotropic condition $|\lambda_1| = |\lambda_2|$ for the two-band model Eq. (3). In general the three Fermi contours are fourfold anisotropic when $\lambda_1 + \lambda_2 \neq 0$ and $\eta \neq 0$, as shown in Fig. 2(a-c), where we plot Fermi contours with fixed $\lambda_{1,2}$ but different a_{\pm} .

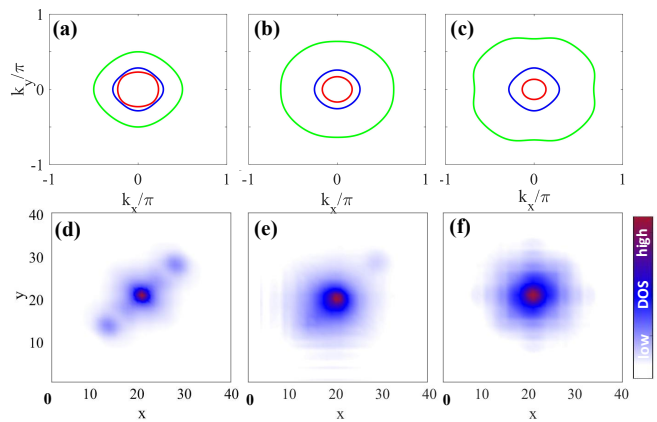


FIG. 2. (a-c) Fermi contours and (d-f) zero-energy density of states in three-band model Eq. (13). Parameters are $\mu = -0.6$, $t = -1$, $\lambda_1 = 0.1$, $\lambda_2 = 0.2$, $t' = -0.3$, $t'' = t'/12$, $\eta = -2$, $M = \beta = 0$ and $\Delta_1 = \Delta_2 = 0.1$, $\Delta_3 = 0.05$. In (a,d) $a_{\pm} = 0$, in (b,e) $a_+ = 0$, $a_- = 0.8$ and in (c,f) $a_{\pm} = 0.8$. In (d-f), three fractional vortices of $\Delta_j(\mathbf{r})$ as modeled by Eq. (11) with $j = 1, 2, 3$ and $\xi = 1$ are placed at $\mathbf{c}_1 = (28, 28)$, $\mathbf{c}_2 = (12, 12)$, and $\mathbf{c}_3 = (20, 20)$, leading to 3 (d), 2 (e) and 1 (f) peaks in zero-energy density of states respectively.

In the superconducting phase A_{1g} , besides $\Delta_{1,2}$ for d_{\pm} -bands, a trivial s -wave spin-singlet pairing order parameter Δ_3 for d_{xy} -band is also included. The pairing Hamiltonian is described by on-site pairings

$$H_{A_{1g}} = \sum_{\mathbf{r}} \Delta_1 d_{+\uparrow} d_{-\downarrow} + \Delta_2 d_{-\uparrow} d_{+\downarrow} + \Delta_3 d_{xy\uparrow} d_{xy\downarrow} + h.c. \quad (16)$$

where the sum is over all lattice sites \mathbf{r} .

Under an out-of-plane magnetic field, fractional vortices of $\Delta_j(\mathbf{r})$ as modeled by Eq. (11) with $j = 1, 2, 3$ and the corresponding VBSs can be induced. In Fig. 2 (d-f) we calculate and plot the zero-energy density of states. When all IBCs are weak, one may expect three peaks localized at the cores of three fractional vortices as shown in Fig. 2(d). As the IBCs increase, VBS peaks at nearest fractional vortices may merge together, resulting in two [Fig. 2(e)] or even one peak [Fig. 2(f)]. Thus, when one vortex is split into three fractional vortices, the observed number of VBS peaks can be one, two or three, depending on the details of IBCs. Our theoretical calculations are consistent with the experiments [24], where VBSs with 1, 2 and 3 peaks have all been observed.

The fractional vortices are induced and stabilized by out-of-plane magnetic fields. In the following we will consider effects of in-plane magnetic fields.

In-plane upper critical field.— When an in-plane magnetic field \mathbf{B} is applied, the orbital effect can be neglected and the Zeeman effect dominates. In the normal state, the three-band Hamiltonian Eq. (13) is modified to con-

tain the Zeeman coupling term

$$H_0(\mathbf{k}) \rightarrow H_0(\mathbf{k}) + \frac{1}{2}\mu_B \hat{g} \mathbf{B} \cdot \mathbf{s}, \quad (17)$$

where μ_B is the Bohr magneton, $\hat{g} = \text{diag}(g_+, g_-, g_3)$ is a matrix in orbital space and g_\pm, g_3 are the Landé g -factors for d_\pm -orbitals and d_{xy} -orbital respectively. Due to time-reversal symmetry, $g_+ = g_- \equiv g$.

In the superconducting state, we need to focus on the Fermi contours where pairing occurs. On the Fermi contour of d_{xy} -band, due to inversion symmetry, there is no SOC in the orbital singlet d_{xy} -band. As a result, the in-plane upper critical field is $2B_{c2}^{\text{BCS}}/g_3$, where B_{c2}^{BCS} is the critical field of a Bardeen-Cooper-Schrieffer (BCS) superconductor purely due to Zeeman effect.

On the Fermi contour of d_\pm -bands, since d_\pm -orbitals form a doublet, there exists Ising SOC as shown in Eqs. (3) and (13). Similar to the effective pairing potentials, the effective Zeeman field on d_\pm -bands can be obtained

$$\mathbf{B}_{\text{eff}} = \frac{\lambda_F}{\sqrt{\lambda_F^2 + \beta_F^2}} \mathbf{B}, \quad (18)$$

where λ_F and β_F are angular averages of IBC and SOC respectively along three Fermi contours (FCs)

$$\lambda_F = \int_{\text{FC}} \frac{d\theta}{2\pi} |\lambda(\mathbf{k})|, \quad \beta_F = \int_{\text{FC}} \frac{d\theta}{2\pi} |\beta(\mathbf{k})|, \quad (19)$$

with θ as the polar angle of \mathbf{k} . According to our previous assumption, we have $|\mu| \gg \lambda_F, \beta_F, \Delta_{1,2}$.

From Eq. (18), the in-plane upper critical field B_{c2} is

$$\frac{B_{c2}}{B_{c2}^{\text{BCS}}} = \frac{2}{g} \sqrt{1 + \left(\frac{\beta_F}{\lambda_F}\right)^2}. \quad (20)$$

In Fig. 3 we work out and plot the self-consistent pairing gap $\Delta = \Delta_1 = \Delta_2$ as a function of temperature T and field B . In the phase diagram, the phase transition line denotes B_{c2} . Without Ising SOC, B_{c2} becomes the BCS critical field $2B_{c2}^{\text{BCS}}/g$, as shown in Fig. 3(a), which increases to the well-known Pauli limit B_P at zero temperature. As shown in Fig. 3(b) and (c), when Ising SOC is nonzero, B_{c2} can bypass the Pauli limit even at nonzero temperatures, and the field enhancement increases with the ratio β_F/λ_F as described in Eq. (20).

Physically, the inversion symmetry is preserved, and the Ising SOC couples spin and orbitals near Γ point. For each orbital, Ising SOC behaves like a Zeeman field along out-of-plane direction, which enhances B_{c2} . For opposite orbitals, Ising SOC are opposite in sign but the same in magnitude, to preserve time-reversal symmetry. However, IBCs $\lambda_{1,2}$ couple opposite orbitals and tend to weaken the spin pinning of Ising SOC for each orbital. As a result, we arrive at the enhancement formula Eq. (20) for the in-plane upper critical field. This is one example of Ising superconductivity [52–55].

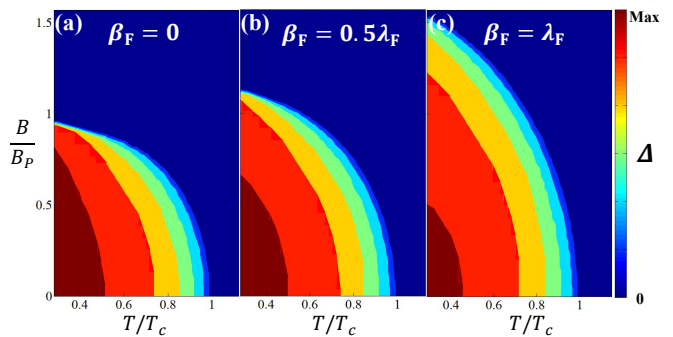


FIG. 3. Phase diagrams with different Ising SOC. The two-band model Eq. (3) is employed with $\mu = -0.6, t = -1, \lambda_1 = 0.1, \lambda_2 = 0.2$, and (a) $\beta = 0$ (b) $\beta = 0.1$ and (c) $\beta = 0.2$.

In our calculations, we assume the Cooper pair momentum is always zero. At low temperatures, finite-momentum pairing states such as Fulde-Ferrell-Larkin-Ovchinnikov phase may arise beyond Pauli limit [56, 57], which could further enhance the in-plane upper critical fields. In particular, in the Fulde-Ferrell phase the inversion symmetry can be spontaneously broken, leading to the potential supercurrent diode effect [58–60].

Conclusion.— In this work, we study the two- and three-band models arising from iron-based superconductors. We analyze the properties of Fermi contours and vortex bound states, which are related to the couplings between different bands. Our results may help to explain the experimental observation of vortex bound states in monolayer iron-based superconductors. We also calculated the in-plane upper critical field self-consistently, and predict Ising superconductivity might be observed in monolayer iron-based superconductors such as $\text{Ba}_{1-x}\text{K}_x\text{Fe}_2\text{As}_2$, LiFeAs and $\text{FeTe}_{1-x}\text{Se}_x$.

Acknowledgements.— We thank Egor Babaev for important discussions. We thank Hong Ding, Baiqing Lv and Quanxin Hu for helpful discussions. This work is supported by the National Natural Science Foundation of China (Grant. No. 12174021).

* fyuanaa@connect.ust.hk

- [1] H. J. Choi, *et al.*, *Nature* **418**, 758 (2002).
- [2] S. Souma, *et al.*, *Nature* **423**, 65 (2003).
- [3] G. Blumberg, *et al.*, *Phys. Rev. Lett.* **99**, 227002 (2007).
- [4] K. H. Jin, H. Huang, J. W. Mei, Z. Liu, L. K. Lim, and F. Liu, *Npj Comput. Mater.* **5**, 57 (2019).
- [5] X. Zhou, *et al.*, *Phys. Rev. B* **100**, 184511 (2019).
- [6] X. Xi, *et al.*, *Nat. Phys.* **12**, 139 (2016).
- [7] W. Y. He, B. T. Zhou, J. J. He, N. F. Q. Yuan, T. Zhang, and Law, *K. T. Commun. Phys.* **1**, 40 (2018).
- [8] D. Shaffer, *et al.*, *Phys. Rev. B* **101**, 224503 (2020).
- [9] S. Kezilebieke, *et al.*, *Nature*, **588**, 424 (2020).
- [10] A. Hamill, *et al.*, *Nat. Phys.* **17**, 949 (2021).
- [11] H. Ding, *et al.*, *Europhysics Letters*, **83**, 47001 (2008).

- [12] T. Qian, *et al.*, Phys. Rev. Lett. **106**, 187001 (2011).
- [13] P. Zhang, *et al.*, Science, **360**, 182 (2018).
- [14] V. Grinenko, *et al.*, Nat. Phys. **16**, 789 (2020).
- [15] V. Grinenko, *et al.*, Nat. Phys. **17**, 1254 (2021).
- [16] I. Shipulin, *et al.*, Nat. Commun. **14**, 6734 (2023).
- [17] S. Deng, L. Viola and G. Ortiz, Phys. Rev. Lett. **108**, 036803 (2012).
- [18] Gang Xu, Biao Lian, Peizhe Tang, Xiao-Liang Qi, and Shou-Cheng Zhang, Phys. Rev. Lett. **117**, 047001 (2016).
- [19] X. Wu, S. Qin, Y. Liang, H. Fan, and J. Hu, Phys. Rev. B, **93**, 115129 (2016).
- [20] E. Babaev, Phys. Rev. Lett. **89**, 067001 (2002).
- [21] F. Wilczek, Phys. Rev. Lett. **48**, 1144 (1982).
- [22] D. Wang, *et al.*, Science, **362**, 333 (2018).
- [23] Y. Iguchi, R. A. Shi, K Kihou, C. H. Lee, M. Barkman, A. L. Benfenati, V. Grinenko, Science **380**, 1244 (2023).
- [24] Y. Zheng, *et al.*, arXiv:2407.18610 (2024).
- [25] M. Sigrist and K. Ueda, Rev. Mod. Phys. **63**, 239 (1991).
- [26] J. Carlström, J. Garaud, and E. Babaev, Phys. Rev. B **84**, 134518 (2011).
- [27] J. Garaud, J. Carlström, E. Babaev, and M. Speight, Phys. Rev. B **87**, 014507 (2013).
- [28] J. Garaud, M. Silaev, and E. Babaev, Phys. C: Supercond. Appl. **533**, 63 (2017).
- [29] M. H. Christensen, B. M. Andersen, and P. Kotetes, Phys. Rev. X, **8**, 041022 (2018).
- [30] A. Maiani, A. Benfenati, and E. Babaev, Phys. Rev. B **105**, 224507 (2022).
- [31] Y. Wang, P. J. Hirschfeld, and I. Vekhter, Phys. Rev. B **85**, 020506 (2012).
- [32] M. Marciiani, L. Fanfarillo, C. Castellani, and L. Benfatto, Phys. Rev. B **88**, 214508 (2013).
- [33] J. Böker, P. A. Volkov, K. B. Efetov, and I. Eremin, Phys. Rev. B **96**, 014517 (2017).
- [34] A. Benfenati, M. Barkman, and E. Babaev, Phys. Rev. B, **107**, 094503 (2023).
- [35] I. Timoshuk and E. Babaev, arXiv:2407.20132(2024).
- [36] S. Graser, *et al.*, Phys. Rev. B **81**, 214503 (2010).
- [37] V. B. Zabolotnyy, *et al.*, Nature, **457**, 569 (2009).
- [38] P. Zhang, *et al.*, Phys. Rev. B **91**, 214503 (2015).
- [39] R. M. Fernandes, and A. V. Chubukov, Rep. Prog. Phys. **80**, 014503 (2016).
- [40] K. Nakayama, *et al.*, Phys. Rev. B **83**, 020501 (2011).
- [41] S. V. Borisenko, *et al.*, Nat. Phys. **12**, 311 (2016).
- [42] Y. S. Kushnirenko, *et al.*, Phys. Rev. B, **102**, 184502 (2020).
- [43] S. Qin, C. Fang, F. C. Zhang, and J. Hu, Phys. Rev. X, **12**, 011030 (2022).
- [44] T. Sato, *et al.*, Phys. Rev. Lett. **103**, 047002 (2009).
- [45] Y. Zhang, *et al.*, Nat. Mater. **10**, 273 (2011).
- [46] N. Xu, *et al.*, Phys. Rev. B **88**, 220508 (2013).
- [47] Y. Ota, *et al.*, Phys. Rev. B, **89**, 081103 (2014).
- [48] D. Wu, *et al.*, Nat. Phys. **20**, 571 (2024).
- [49] B. A. Bernevig, T. L. Hughes, and S. C. Zhang, Science **314**, 1757 (2006).
- [50] E. I. Rashba and V. I. Sheka, Fiz. Tverd. Tela: Collected Papers **2**, 162 (1959).
- [51] Y. A. Bychkov and E. I. Rashba, J. Phys. C **17**, 6039 (1984).
- [52] J. M. Lu, *et al.*, Science **350**, 1353 (2015).
- [53] X. Xi, *et al.*, Nat. Phys. **12**, 139 (2016).
- [54] J. Falson, *et al.*, Science **367**, 1454 (2020).
- [55] H. Liu, H. Liu, D. Zhang, and X. C. Xie, Phys. Rev. B **102**, 174510 (2020).
- [56] P. Fulde and R. A. Ferrell, Phys. Rev. **135**, A550 (1964).
- [57] A. I. Larkin and Yu. N. Ovchinnikov, Sov. Phys. JETP **20**, 762 (1965).
- [58] Noah F. Q. Yuan and Liang Fu, PNAS **119** (15) e2119548119 (2022).
- [59] Akito Daido, Yuhei Ikeda, and Youichi Yanase, Phys. Rev. Lett. **128**, 037001 (2022).
- [60] James Jun He, Yukio Tanaka, and Naoto Nagaosa, New J. Phys. **24**, 053014 (2022).